Dirac-cone induced gating enhancement in single-molecule field-effect transistors

Hantao Sun[1, 2], Xunshan Liu[3], Yanjie Su[1,2], Bing Deng[4], Hailin Peng[4], Silvio Decurtins[3], Stefano Sanvito[5], Shi-Xia Liu[3, *], Shimin Hou[1, 2, *], Jianhui Liao[1, *]

[1]Key Laboratory for the Physics and Chemistry of Nanodevices, Department of Electronics, Peking University, Beijing 100871, China

[2]Centre for Nanoscale Science and Technology, Peking University, Beijing 100871, China

[3]Departement für Chemie und Biochemie, Universität Bern, Freiestrasse 3, 3012 Bern, Switzerland

[4]Center for Nanochemistry, Beijing National Laboratory for Molecular Sciences (BNLMS), College of Chemistry and Molecular Engineering, Peking University, Beijing 100871, China

[5]School of Physics, AMBER and CRANN Institute, Trinity College, Dublin 2, Ireland

* The corresponding authors. E-mail: shi-xia.liu@dcb.unibe.ch; smhou@pku.edu.cn; jianhui.liao@pku.edu.cn

1. Synthesis of the amine-terminated BDF derivative

BDF derivatives have received tremendous attention due to their fascinating redox and optical properties. The synthesis of the target amine-terminated BDF derivative was accomplished in 63% yield *via* a Sonogashira reaction of 2,6-Bis(N, N-dihexylamino)-4,8-diiodobenzo[1, 2-*b*:4, 5-*b'*]-difuran-3,7-dicarbonitrile with 4-ethynylaniline. All the chemicals and solvents were purchased from commercial sources and were used without further purification. 2,6-Bis(N, N-dihexylamino)-4,8-diiodobenzo[1,2-b:4,5-b']difuran-3,7-dicarbonitrile was synthesized according to the literatures [1, 2]. 1H and 13C NMR spectra were obtained on a Bruker AC 300 spectrometer operating at 400 MHz and 100 MHz, respectively.

A mixture of 2,6-bis(N,N-dihexylamino)-4,8-diiodobenzo[1,2-b:4,5-b']difuran-3,7-dicarbonitrile (165 mg, 0.2 mmol) and 4-ethynylaniline (47 mg, 0.4 mmol) in Et3N (20 mL) / piperidine (1 mL) was added Pd(PPh3)2Cl2 (28 mg, 0.04 mmol), and CuI (8 mg, 0.04 mmol). The mixture was purged with N2 for 20 min and stirred at 110 °C for 12 h. After cooling down to room temperature, the resultant yellow precipitate was filtrated off, washed with methanol and dried in vacuo. The crude product was purified by chromatography on a silica gel using

dichloromethane/ethyl alcohol (50:1) as eluent to afford analytically pure product as a yellow solid (101 mg, yield 63%). 1H NMR (DMF-d7) δ: 7.46 (d, J = 8.32 Hz, 4 H), 6.75 (d, J = 8.40 Hz, 4 H), 5.48 (s, 4 H), 3.75 (t, J = 7.56 Hz, 8 H), 1.86 (m, 8 H), 1.51-1.35 (m, 24 H), 0.91 (t, J = 7.04 Hz, 12 H). 13C NMR (DMF-d7) δ: 164.50, 151.42, 145.91, 133.82, 123.60, 117.13, 115.02, 110.76, 103.03, 97.14, 78.50, 51.18, 32.45, 29.47, 27.14, 23.44, 14.48. MALDI-TOF MS: Calcd for C52H64N6O2 [M]+ 804.51, found: 804.27.

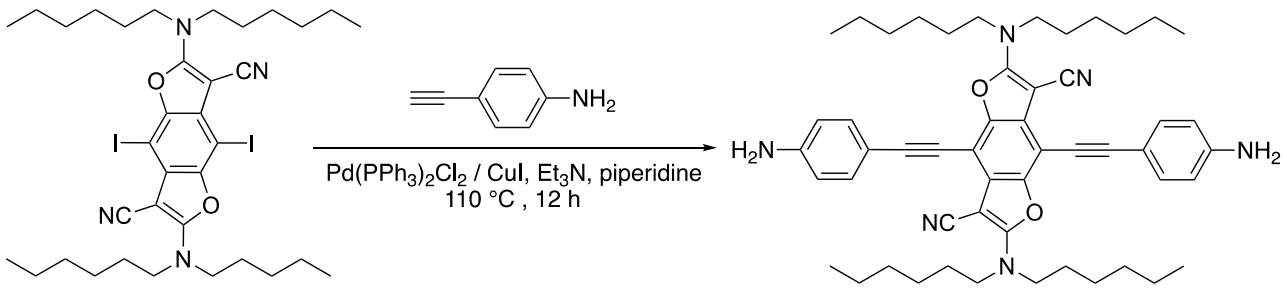

Scheme 1. A synthetic route to the target amine-terminated BDF derivative.

2. Electronic characterization of graphene devices

Single-layer graphene grown by chemical vapor deposition on copper was transferred onto pre-patterned local gate with an electrolytic bubbling transfer method [3]. We characterized the graphene structure before the electroburning process. Figure S1a shows the current-voltage curves measured at room temperature for different gate voltages. As we can see, the gate electrode efficiently modulates the charge transport in graphene. Thanks for the high purity of graphene and the clean transfer process, our graphene devices work around the Dirac point at V_g=0 *V,* as illustrated in the transfer curve measured at the fixed bias voltage V_{ds}=0.1 *V* (the black line in Figure S1b). Moreover, we examined the impact of the molecule deposition process on graphene. After several hours of immersion in the BDF pyridine solution, our graphene devices did not show any significant changes (the red line in Figure S1b). Figure S1c shows the leakage current of the bottom-gate. The bottom-gate made of $Al/Al_2O_3/HfO_2$ is robust with a very low leakage current less than 2 *pA,* which is suitable for single-molecule FETs.

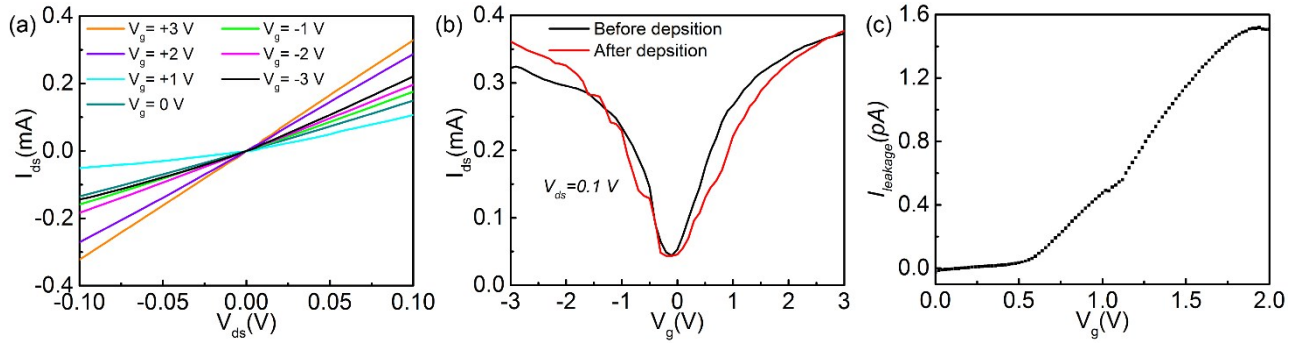

Figure S1. Electronic characterization of single-layer graphene structures before the electroburning process. **a,** Typical current-voltage curves of graphene devices measured at room temperature for different gate voltages. **b,** The corresponding transfer curves measured at the fixed bias voltage V_{ds}=0.1 V before (black line) and after (red line) the BDF deposition process. The graphene is nearly intrinsic as the Dirac point appears near the zero gate voltage. **c,** The leakage current of the bottom gate made of $Al/Al_2O_3/HfO_2$.

3. Control experiment for molecule connection

In order to verify the connection of the targeted BDF molecules, we have performed a control experiment in which 100 devices were fabricated using the same assembly process in an anhydrous pyridine solution without the targeted BDF molecules. As expected, we did not observe a large current increase in these devices. Then we performed statistical analysis on the low-bias conductance of these dvices (it should be noted that some devices did not show any detectable electric current). Comparison of the low-bias conductance values between these devices and the graphene-BDF-graphene molecular junctions is shown in Figure S2. Obviously, the conductance values of these devices are always much less than those of the graphene-BDF-graphene molecular junctions.

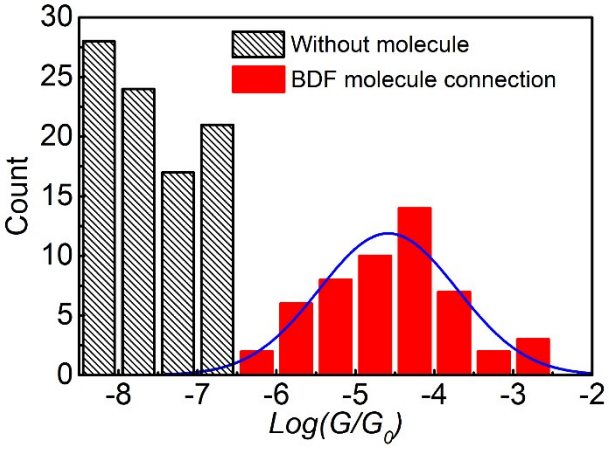

Figure S2. Comparison of the low-bias conductance values between the devices fabricated in the control experiment and the graphene-BDF-graphene molecular junctions.

4. Experimental data of other single-molecule FETs with obvious gating effects

In the experiments, we observed reproducible gating effects as discussed in the main text. Figure S3 presents the current-voltage characteristics and the corresponding transfer curves of other three devices (D, E, F) with ambipolar conduction. The performance of these three devices is very similar to that of Device B.

Figure S4 shows the current-voltage characteristics of Device G measured at 77 K for different gate voltages and the transfer curve measured at the fixed bias voltage V_{ds}=-0.4 V. In the positive gate voltage regime, the electric current is almost independent on the gate voltage, which is in good agreement with that of Device C.

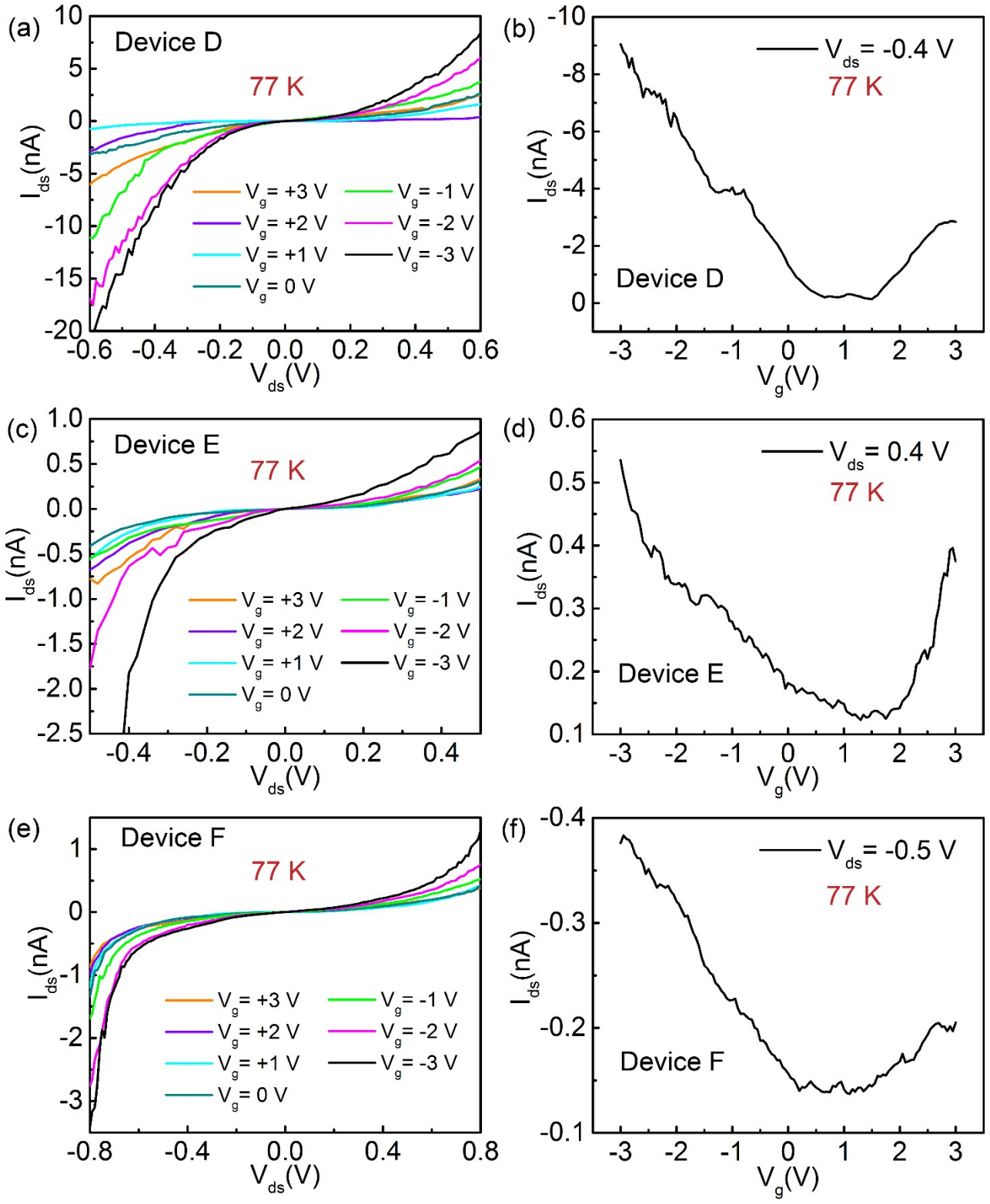

Figure S3. Ambipolar conduction of single-molecule FETs (Devices D, E and F). (**a, c, e**) Current-voltage characteristics measured at 77 K for different gate voltages. (**b, d, f**) The corresponding transfer curves measured at the fixed bias voltage of V_{ds}=-0.4 V (**b**), 0.4 V (**d**) and -0.5 V (**f**).

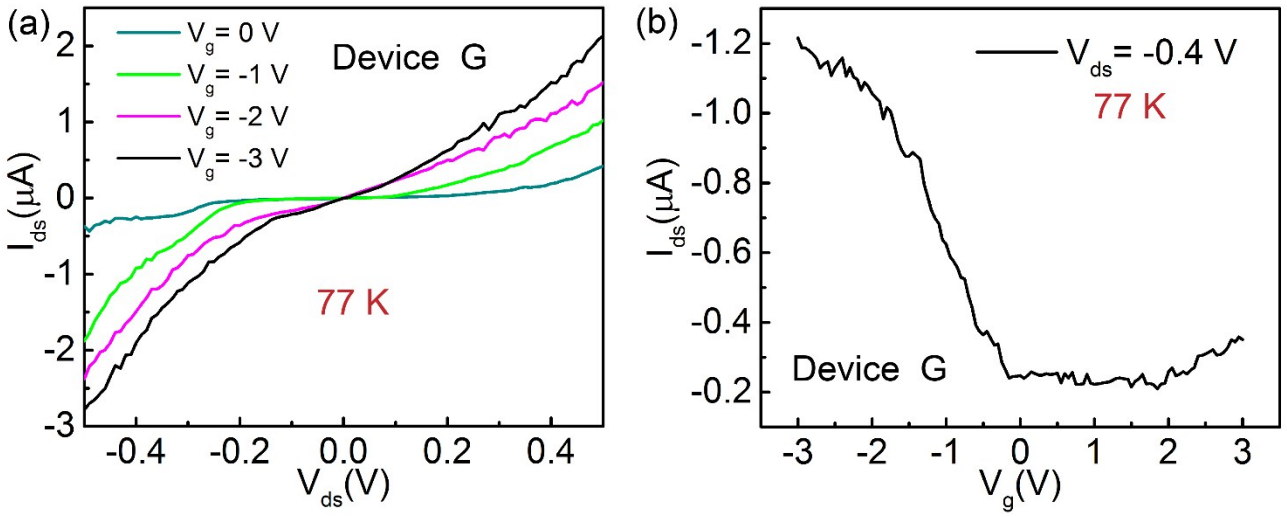

Figure S4. **a,** Current-voltage characteristics of Device G measured at 77 K for different gate voltages, **b,** the corresponding transfer curve measured at the fixed bias voltage V_{ds}=-0.4 *V*.

5. Transition voltage analysis of the modified single-level model incorporating the graphene states

We observed an abnormal gate-dependent behavior of the transition voltage in Device B, which was assumed to be induced by the electrostatic gating on the graphene leads. To get a deep insight, we calculate the transition voltages with the modified single-level model in different situations by changing the gate efficiency factors. Simulation parameters, ε_0=*-0.43 eV*, Γ_S=*1.0 meV* and Γ_D=*1.1 meV*, are obtained from fitting the experimental *I-V* data of Figure 1c. First of all, we choose α_1=*0* and α_2=*0.06* to simulate the situation that the electrostatic gating only affects the HOMO. The current-voltage characteristics calculated at different gate voltages and the corresponding F-N plots are shown in Figures S5a and S5b, respectively. As expected, the transition voltage decreases monotonically (as pointed out by the blue arrows in Figure S5b) when the HOMO is shifted upwards by the applied gate voltage sweeping from V_g=*+3 V* to V_g=*-3 V*. Then, we set α_1=*0.02* and α_2=*0.06* to add a tiny electrostatic gating on the graphene leads. While the current-voltage curves calculated at different gate voltages still demonstrate HOMO-dominated transport characteristics (Figure S5c), the transition voltage displays a vastly different behavior in the negative gate polarity (the blue arrows in Figure S5d). In contrast to the HOMO that moves upwards, the transition voltage starts to increase when the gate voltage becomes increasingly negative, which is a direct evidence of the huge impact on the transition voltage associated with the electrostatic gating on the graphene leads. The electrostatic gating on the graphene leads changes their DOS contributing to

the electron conduction (Figure S5e). At zero gate voltage, the DOS of the graphene leads in the bias window is a quadratic function of the bias voltage (Figure S5f). In contrast, the negative gate voltage shifts upwards the Dirac point and only the p-branch is included into the bias window at lower bias voltages, so that the DOS of the graphene leads in the bias window increases linearly following the increase of the bias. Until the bias voltage is large enough to include the Dirac point into the bias window, the DOS of the graphene leads contributing to the conduction quadratically increases again.

At last, we analyze the transition voltage of the single-level model in the typical situation that the electrostatic gating on the graphene leads dominates the charge transport. Figures S6a and S6b present the corresponding F–N plots of the calculated current-voltage curves shown in Figure 4g. As we can see, the transition voltages scale up for both the positive and negative gate voltage polarities (as pointed out by the blue arrows), in excellent agreement with the measured behavior of Device B.

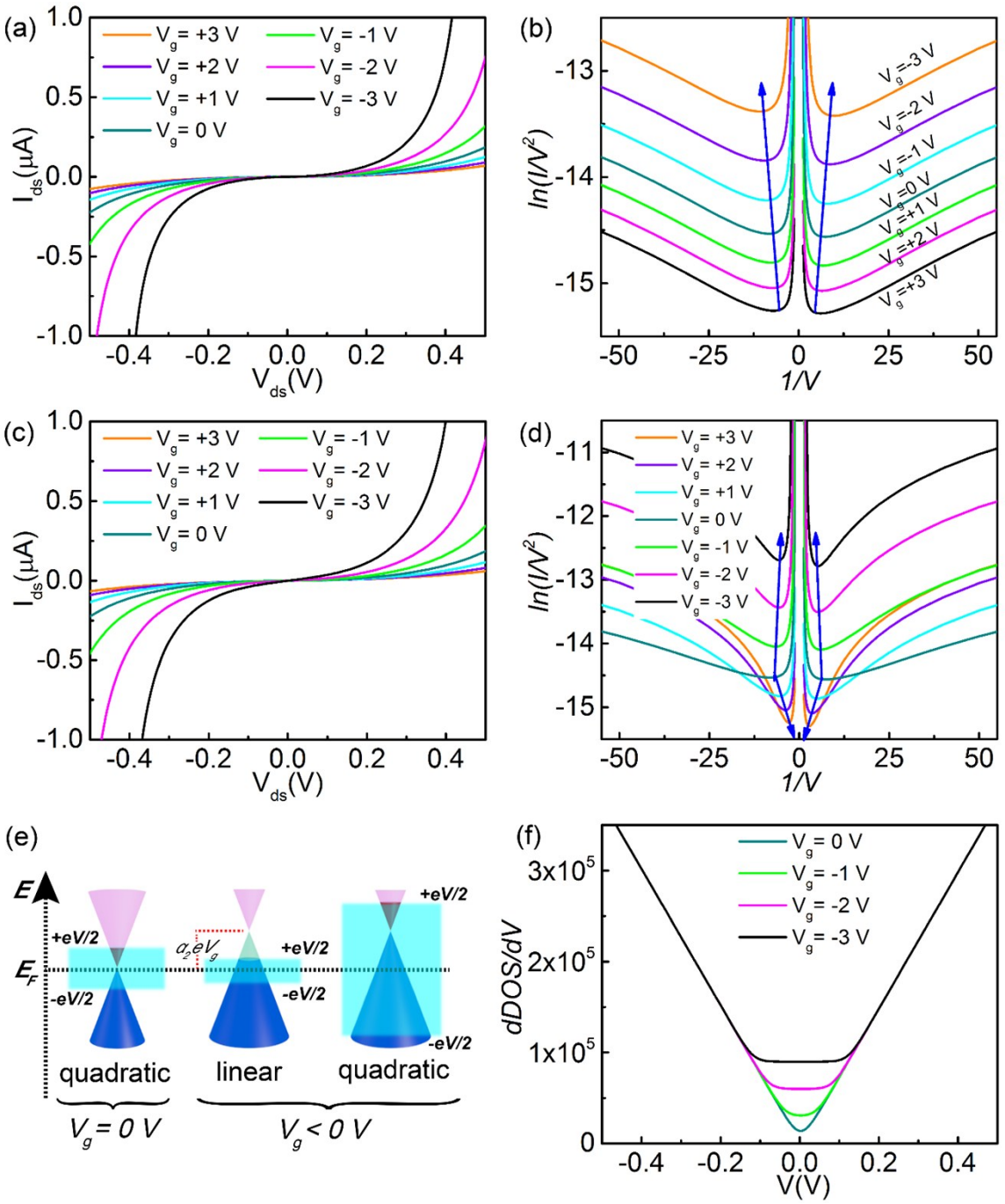

Figure S5. Transition voltage analysis using the modified single-level model with the electrostatic gating mainly affecting the HOMO. The current-voltage curves calculated at different gate voltages (**a**) and the corresponding F-N plots (**b**) for the specific situation that the electrostatic gating only affects the HOMO, which is simulated with $\alpha_1=0$ and $\alpha_2=0.06$. The current-voltage curves (**c**) and the corresponding F–N plots (**d**) when added with a tiny electrostatic gating on the graphene leads, which is simulated with $\alpha_1=0.02$ and $\alpha_2=0.06$. (**e**) The schematic of the effects of the applied gate voltage on the DOS of the graphene leads in the bias window. (**f**) The derivative of the DOS of the graphene leads in the bias window as a function of the bias voltage.

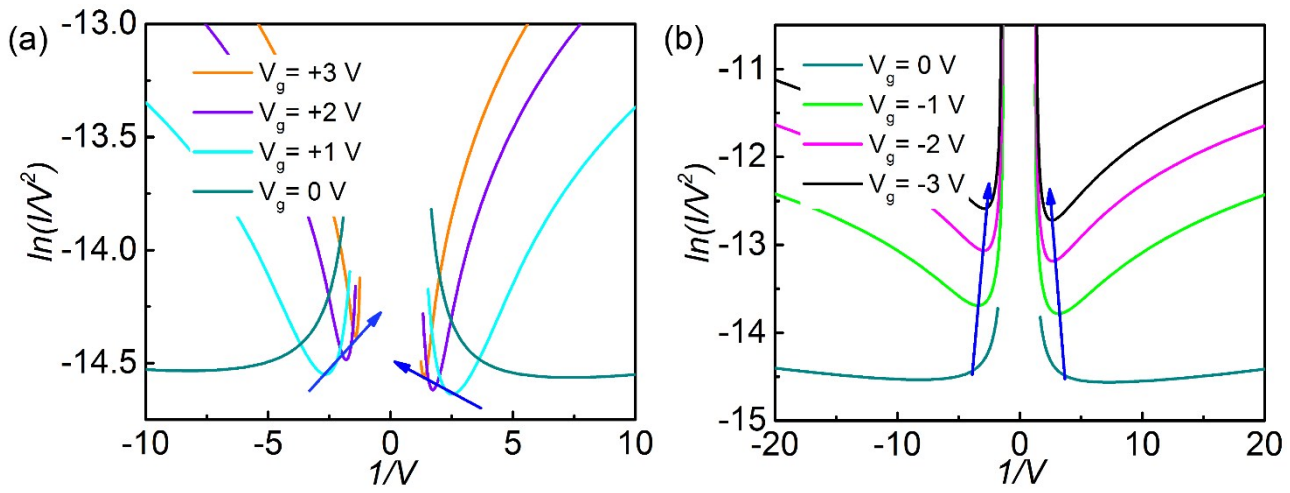

Figure S6. Transition voltage analysis of the single-level model with the electrostatic gating mainly affecting the graphene leads. The corresponding F–N plots of the calculated current-voltage curves shown in Figure 4g at the positive (**a**) and negative (**b**) gate polarities, which is simulated with α_1=*0.1* and α_2=*0.02*.

6. Single-molecule FETs with chemically doped graphene leads

To improve the performance of single-molecule FETs, we perform simulations using the modified single-level model with chemically doped graphene leads. We use p-type doped graphene as the leads for a p-type (HOMO-dominated) single-molecule FET, in which the two key simulation parameters are chosen as E_{Dirac}=*0.3 eV* and ε_0=*-0.43 eV*. Other simulation parameters were obtained from the fitting of the experimental *I-V* data in Figure 1c. Three typical situations are simulated: (1) the electrostatic gating only affects the HOMO, which is simulated with α_1=*0* and α_2=*0.06*; (2) the electrostatic gating only affects the graphene leads, which is simulated with α_1=*0.1* and α_2=*0*; (3) the electrostatic gating affects both the HOMO and the graphene leads, which is simulated with α_1=*0.1* and α_2=*0.06*. The calculated current-voltage characteristics at different gate voltages, the transfer curve at the fixed bias voltage V_{ds}=*-0.2 V* and the corresponding transconductance are shown in Figure S7. Clearly, the electrical characteristics always exhibit p-type behavior and the electrostatic gating on the graphene leads enhances the gating effects of the single-molecule FET in the entire operating regime. The use of the p-type doped graphene not only increases the transconductance but also suppresses ambipolar conduction.

The same goes for the n-type (LUMO-dominated) single-molecule FET with n-type doped graphene as the leads. The corresponding calculation results are shown in Figure S8, which are

obtained with E_{Dirac}=*-0.3 eV* and ε_0=*0.43 eV*. The electrical characteristics always exhibit n-type behavior and gating enhancement is observed in the entire operating regime.

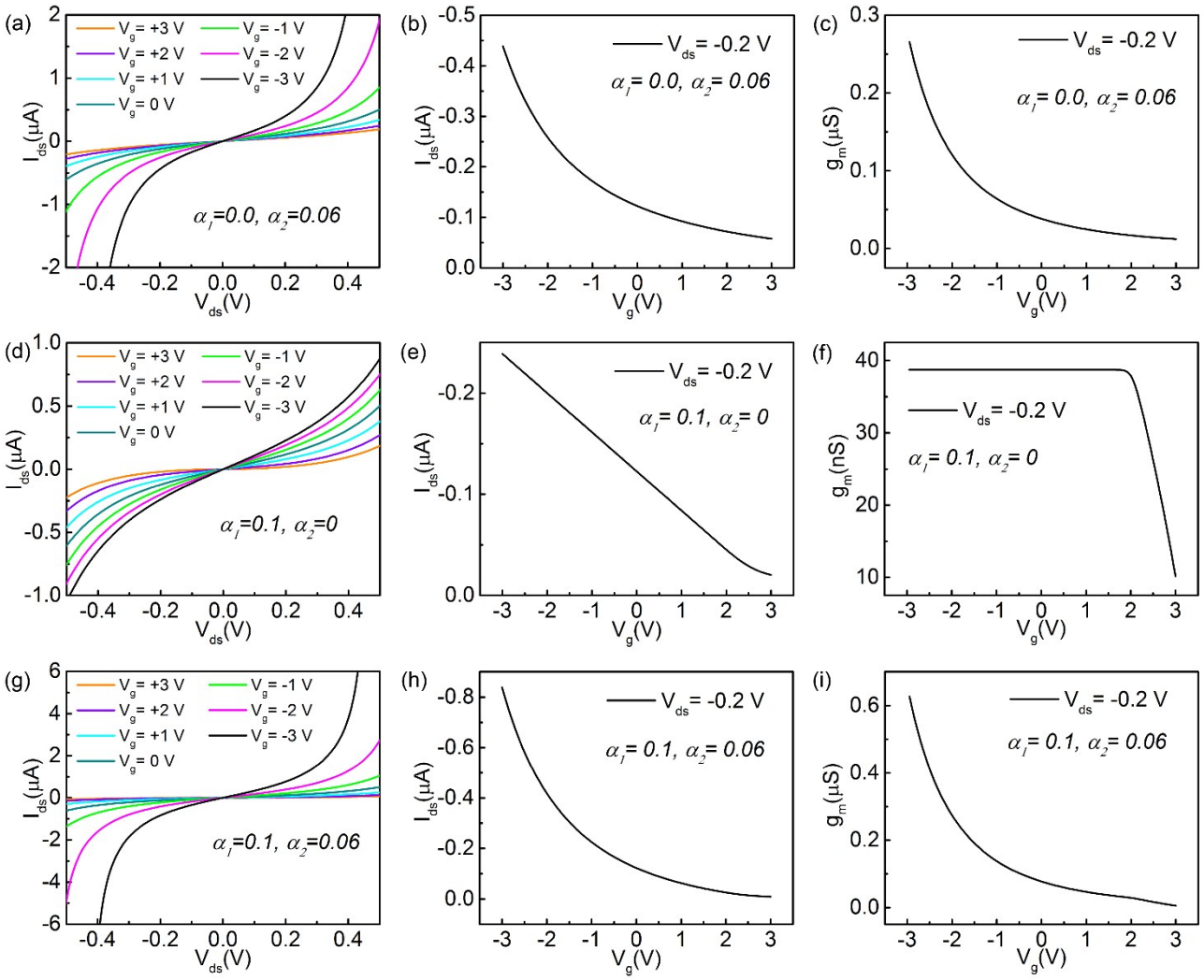

Figure S7. Theoretical modeling of the p-type (HOMO-dominated) single-molecule FET with p-type doped graphene leads. Three typical situations are simulated. The calculated current-voltage characteristics at different gate voltages (**a, d, g**), the transfer curves at the fixed bias voltage V_{ds}=*-0.2 V* (**b, e, h**) and the corresponding transconductances (**c, f, i**) are shown. **a-c,** the electrostatic gating only affects the HOMO, which is obtained with α_1=*0* and α_2=*0.06*. **d-f,** the electrostatic gating only affects the graphene leads, which is obtained with α_1=*0.1* and α_2=*0*. **g-i,** the electrostatic gating affects both the HOMO and the graphene leads, which are obtained with α_1=*0.1* and α_2=*0.06*.

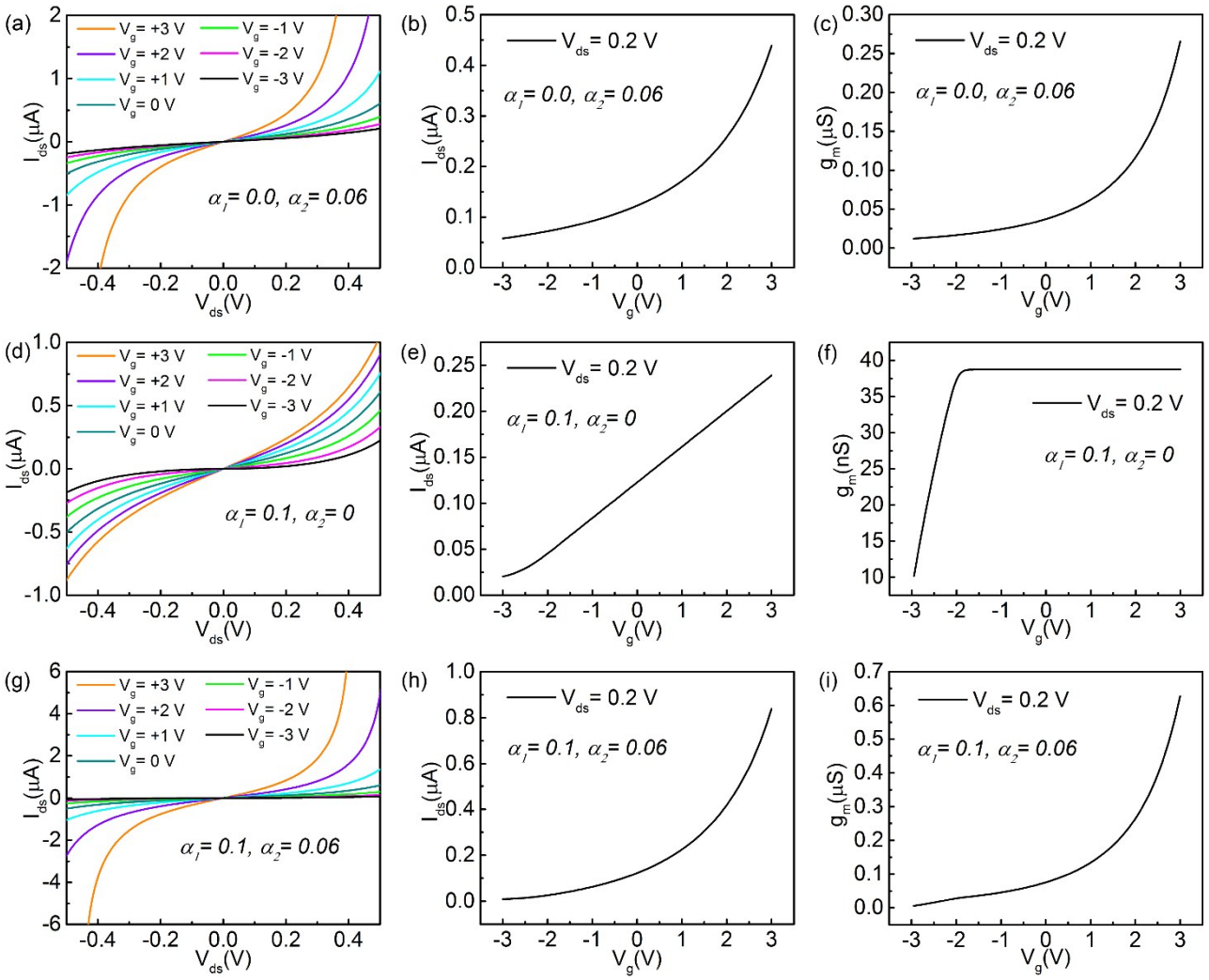

Figure S8. Theoretical modeling of the n-type (LUMO-dominated) single-molecule FET with n-type doped graphene leads. Three typical situations are simulated, and the calculated current-voltage characteristics at different gate voltages (**a, d, g**), the transfer curves at the fixed bias voltage $V_{ds}=0.2\ V$ (**b, e, h**) and the corresponding transconductances (**c, f, i**) are shown. **a-c,** the electrostatic gating only affects the LUMO, which is obtained with $\alpha_1=0$ and $\alpha_2=0.06$. **d-f,** the electrostatic gating only affects the graphene leads, which is obtained with $\alpha_1=0.1$ and $\alpha_2=0$. **g-i,** the electrostatic gating affects both the LUMO and the graphene leads, which is obtained with $\alpha_1=0.1$ and $\alpha_2=0.06$.

References

1. Li, H., Jiang, P., Yi, C., Li, C., Liu, S.-X., Tan, S., Zhao, B., Braun, J., Meier, W., Wandlowski, T. & Decurtins, S. Benzodifuran-Based pi-Conjugated Copolymers for Bulk Heterojunction Solar Cells. *Macromolecules* **43**, 8058-8062 (2010).
2. Yi, C. Y., Blum, C., Lehmann, M., Keller, S., Liu, S. X., Frei, G., Neels, A., Hauser, J., Schürch, S. & Decurtins, S. Versatile Strategy To Access Fully Functionalized Benzodifurans: Redox-Active Chromophores for the Construction of Extended pi-Conjugated Materials. *J. Org. Chem.* **75**, 3350-3357 (2010).
3. Gao, L., Ren, W., Xu, H., Jin, L., Wang, Z., Ma, T., Ma, L.-P., Zhang, Z., Fu, Qiang, Peng, L.-M., Bao, X. & Cheng, H.-M. Repeated growth and bubbling transfer of graphene with millimetre-size single-crystal grains using platinum. *Nat. commun.* **3**, 699 (2012)